



Imaging of OAM-entangled photon pairs in the Bessel-Gauss basis with full index control

ZEFERINO IBARRA-BORJA,¹ ROBERTO RAMÍREZ-ALARCÓN,^{1,*} 
CARLOS SEVILLA-GUTIÉRREZ,¹ HECTOR CRUZ-RAMÍREZ,² AND
ALFRED B. U'REN² 

¹Centro de Investigaciones en Óptica A.C., Loma del Bosque 115, Colonia Lomas del Campestre, 37150 León Guanajuato, Mexico

²Instituto de Ciencias Nucleares, Universidad Nacional Autónoma de México, Apartado Postal 70-543, 04510 DF, Mexico

*roberto.ramirez@cio.mx

Abstract: In this paper, we directly image the orbital angular momentum (OAM) correlations, expressed in the Bessel-Gauss (BG) basis, present in quantum-entangled photon pairs produced by the process of spontaneous parametric downconversion (SPDC). We use a spatial light modulator that displays an appropriate phase mask, followed by coupling into a single-mode fiber, so as to project the signal, or heralding, photon onto a BG mode, and verify that the idler, or heralded, photon is projected non-locally as expected. In contrast with similar experiments relying on Laguerre-Gauss (LG) modes, our current experiment permits, firstly, full index control (allowing the experimenter to define both the azimuthal index ℓ_s and the continuous radial index k_{rs} , also referred to as scaling parameter). Importantly, while not resolving the radial index leaves the heralded single photon in a statistical mixture of all available radial modes, the ability to determine both indices allows us to herald single photons in a particular BG mode, described by a quantum-mechanically pure state. Our use of BG modes permits, secondly, the spatially-resolved detection of the heralded single photon, both in the near and far fields, with a time-gated intensified CCD camera, making it possible to experimentally determine both the radial and azimuthal indices of the heralded single photon. Thirdly, the fact that for BG modes the radial index (scaling parameter) is continuous makes it possible to use the scaling parameter as a continuous adjustment in quantum state engineering, for precise mode matching, or for the selection of photon-pair properties such as the spiral bandwidth, as we experimentally demonstrate. We believe that our work opens up interesting new possibilities in the field of quantum communications based on the spatial degree of freedom of photon pairs.

© 2021 Optical Society of America under the terms of the [OSA Open Access Publishing Agreement](#)

1. Introduction

Quantum entanglement is one of the most intriguing features of quantum mechanics and forms the basis for the development of next-generation technologies, such as quantum communications [1–3], quantum computation [4–6], and quantum imaging [7–10]. While the early development of quantum communication protocols exploited polarization entanglement [11,12], the spatial degree of freedom expressed discretely through the orbital angular momentum (OAM), is highly promising since it permits straightforward scaling to higher dimensions, in contrast to polarization which is limited to a dimension of 2.

Spontaneous parametric down conversion (SPDC) represents the process of choice for the generation of photon pairs correlated or entangled in their OAM degree of freedom. Each of the three waves, pump (p), signal (s), and idler (i), involved in the SPDC process may exhibit OAM, as quantified by the topological charge ℓ_μ with $\mu = p, s, i$. Under conditions of azimuthal symmetry, OAM is conserved [13–15] i.e. $\ell_p = \ell_s + \ell_i$, and the resulting two-photon quantum state presents entanglement. Thus, for the pump with a specific topological charge ℓ_p , the state

is a coherent superposition of $|\ell_s\rangle_s|\ell_p - \ell_s\rangle_i$, over a range of ℓ_s values. The Laguerre-Gauss (LG) mode family has been used as basis in a number of relevant experiments which explore OAM photon pair correlations and entanglement [16–23]. Spatial light modulators (SLM's) have been successfully used in some of these works for displaying appropriate phase masks which can project the signal and idler photons to particular modes and thus probe the underlying correlations [23]. Nevertheless, it is experimentally challenging to obtain phase-only masks yielding LG modes with arbitrary values of both the azimuthal index ℓ (corresponding to the topological charge), and the radial index p [18,24]. In most SPDC experiments to date using LG modes and SLM's, a helical phase holographic mask $\exp(-i\ell\phi)$ is used to convert an LG mode field component with the opposite phase $\exp(i\ell\phi)$ to a an $\ell = 0$ mode (Gaussian mode) which can couple well into a single mode fiber. In this manner one can selectively project the incoming field to a desired ℓ value. An important caveat, is that through this approach the resulting projected mode is left in an uncontrolled statistical mixture of modes with different p values (and a fixed ℓ value). It therefore becomes impossible to address an arbitrary LG mode, as defined by particular values of both indices ℓ and p , with the resulting inability to exploit the full LG basis for quantum communication protocols.

Of course, we have the freedom to choose a different basis in which to perform our experiment. In this paper we show that the Bessel-Gauss (BG) mode family leads to some key advantages over LG modes. First, by switching to the BG mode family we are now able to define an appropriate SLM phase mask which allows us to determine both indices, the continuous radial scaling parameter k_r , as well as the azimuthal index ℓ . Defining both indices allows us to herald single photons in a single, well-defined BG mode, described by a quantum-mechanically pure quantum state, to be possibly used in a wide variety of quantum communications protocols. Second, BG modes have a particularly simple angular spectrum morphology (in the form of a single intensity ring with its radius in transverse momentum coordinates equal to the scaling parameter k_{rs}). This implies that from a spatially-resolved, far-field measurement of the heralded photon it becomes possible to directly experimentally access the scaling parameter k_{rs} , complementing a near-field measurement from which the absolute value of the azimuthal index can be obtained. Third, the fact that the radial index (scaling parameter) is continuous makes it possible to use it as a continuous adjustment in quantum state engineering, for precise mode matching, or for the selection of photon-pair properties; indeed, we experimentally demonstrate in this paper how the scaling parameter can be used, in conjunction with the SPDC crystal length and pump focusing strength, to control the resulting spiral bandwidth.

In this paper we thus extend previous work from our group in which we directly imaged the OAM correlations in the two-photon state generated by type-I SPDC [25]. We project the signal (heralding) photon onto a specific BG mode (defined by user-selected radial and azimuthal indices), and spatially-resolve, using a time-gated intensified CCD camera [26–28], the idler (heralded) in both the near and far fields. Our work explores further the capabilities of spatially-resolved detection schemes at the single photon level, which we believe will be useful in future implementations of free-space quantum communications and quantum information technologies.

2. Theory

The process of type-I spontaneous parametric down conversion (SPDC) in a collinear configuration conserves orbital angular momentum (OAM) if the experimental arrangement allows for the collection of all the emitted wavevectors [25,29,30], i.e. $\hbar\ell_p = \hbar\ell_s + \hbar\ell_i$ is satisfied for the pump(p), signal(s) and idler(i) photons carrying OAM values of $\hbar\ell_j$, with $j = p, s, i$, where ℓ_j is the azimuthal index for each of the three fields. It is then natural to decompose the two-photon state in a rotational symmetric basis. In this work we will exploit the Bessel-Gauss (BG) family

of modes as basis, by writing the quantum state as [26]

$$|\Psi\rangle_{SPDC} = \sum_{\ell_s} \sum_{\ell_i} \int \int dk_{rs} dk_{ri} C_{\ell_s, \ell_i}(k_{rs}, k_{ri}) |\ell_s, k_{rs}\rangle |\ell_i, k_{ri}\rangle, \quad (1)$$

where $|\ell_j, k_{rj}\rangle_j$ represents a single photon created in an BG mode with azimuthal index ℓ_j and transverse wavenumber or radial scaling parameter k_{rj} , for the signal (s) or idler (i) modes ($j = s, i$). The coefficients $|C_{\ell_s, \ell_i}(k_{rs}, k_{ri})|^2$ represent the probability of creating a signal photon mode in state $|\ell_s, k_{rs}\rangle_s$ and an idler photon mode in state $|\ell_i, k_{ri}\rangle_i$. Experimentally, it is straightforward to select specific values for the radial scaling parameters k_{rs} and k_{ri} , as we will do in our setup (see below), reducing the two-photon state to

$$|\Psi\rangle_{SPDC}^{k_{rs}, k_{ri}} = \sum_{\ell_s} \sum_{\ell_i} C_{\ell_s, \ell_i} |\ell_s\rangle_s |\ell_i\rangle_i, \quad (2)$$

which, for the case of a Gaussian pump beam ($\ell_p = 0$), as considered in our experiment, Eq. (2) further reduces the two-photon state to

$$|\Psi\rangle_{SPDC}^{k_{rs}, k_{ri}} = \sum_{l=0}^{\infty} (C_{l, -l} |l\rangle_s | -l\rangle_i + C_{-l, l} | -l\rangle_s |l\rangle_i). \quad (3)$$

A Bessel-Gauss beam can be defined as a conical superposition of Gaussian beams, characterized by a beam waist parameter ω_0 , with a cone opening half-angle $\arcsin(k_r/k)$, where k is the wavenumber and k_r is the transverse wavenumber. For a BG beam of order ℓ as experimentally observed in the near-field, the transverse amplitude as a function of the propagation distance z and in terms of the polar coordinates $\{\rho^\perp, \phi\}$, can be written as follows [31,32]

$$BG_\ell(\rho^\perp, \phi) = A \frac{1}{\mu} \exp \left\{ -\frac{1}{\mu} \left(\frac{ik_r^2 z}{2k} \right) + \frac{|\rho^\perp|^2}{\omega_0^2} \right\} \times \mathbf{J}_\ell \left(\frac{k_r |\rho^\perp|}{\mu} \right) \exp(i\ell\phi) \quad (4)$$

where $\mu = 1 + z/z_R$ with $z_R = kw_0^2/2$ is the Rayleigh length, A is a normalization constant, and $\mathbf{J}_\ell(\cdot)$ is an l th Bessel function of the first kind. For the BG basis modes, the transverse wave number k_r acts as the radial index which, in contrast to the p index of the LG modes, can be varied continuously allowing for a finer control of the OAM components present in the two-photon entangled state.

In the far-field, the angular spectrum (AS) of the BG beams presents a characteristic ring shaped transverse intensity distribution, as described by

$$S_\ell(\mathbf{k}^\perp) = A' \exp \left(-\frac{\omega_0^2}{4} |\mathbf{k}^\perp|^2 \right) \times \mathbf{I}_\ell \left(-\frac{k_r \omega_0^2 |\mathbf{k}^\perp|}{2} \right) \exp(i\ell\phi), \quad (5)$$

in terms of the transverse wavevector $\mathbf{k}^\perp (k_x, k_y)$, the normalization constant A' , and the ℓ th order modified Bessel function of the first kind $\mathbf{I}_\ell(\cdot)$, where $\phi = \arctan(k_y/k_x)$. An interesting property of BG beams is that the radius of their ring-shaped angular spectrum directly yields the radial scaling parameter k_r , which together with the azimuthal index ℓ , characterizes the BG family of modes used to decompose the entangled two-photon state [33].

Note that Bessel Gauss beams (as opposed to Bessel beams) are defined by the width of the Gaussian envelope w_0 , in addition to the azimuthal and radial indices. The angular spectrum (i.e. the intensity pattern in the far-field) is characterized by a single intensity ring with its

radius in transverse momentum space equal to the scaling parameter k_{rs} , and its width inversely proportional to w_0 , according to $w_0 = 4/\delta k$, where δk is the ring width. Therefore, the width of the Gaussian envelope can be conveniently retrieved from an experimental measurement of the angular spectrum (obtained as the far-field intensity pattern).

In this work we use a spatially-resolved heralded single photon detection scheme to directly observe the idler-photon transverse distribution in the near-field and in the far-field, while projecting the entangled two-photon state in the Bessel-Gauss basis, as described by Eq. (4) and Eq. (5) respectively.

3. Experiment

The experimental setup is shown in Fig. 1. A diode laser (PL) at 405.2nm is used to pump a β barium borate (BBO) crystal to produce collinear degenerate photon pairs via type-I spontaneous parametric down conversion (SPDC). The pump beam is spatially-filtered by coupling through an aspheric lens (AL_1) into a single mode fiber (SMF₁) and subsequent outcoupling, with a second aspheric lens (AL_2) back into free space. The resulting spatially-filtered beam pass a half wave plate (HWP) for fine adjustment of the linear polarization orientation and is then focused into the crystal, defining a spot size of radius w_0 (as controlled by the focal length of the lens used, labelled as L_1). In the experiments described below, we have used two source configurations: configuration A, involving a BBO crystal of length $L = 2\text{mm}$ and a pump spot size of $w_0 = 300\mu\text{m}$, and configuration B, involving $L = 1\text{mm}$ and $w_0 = 600\mu\text{m}$.

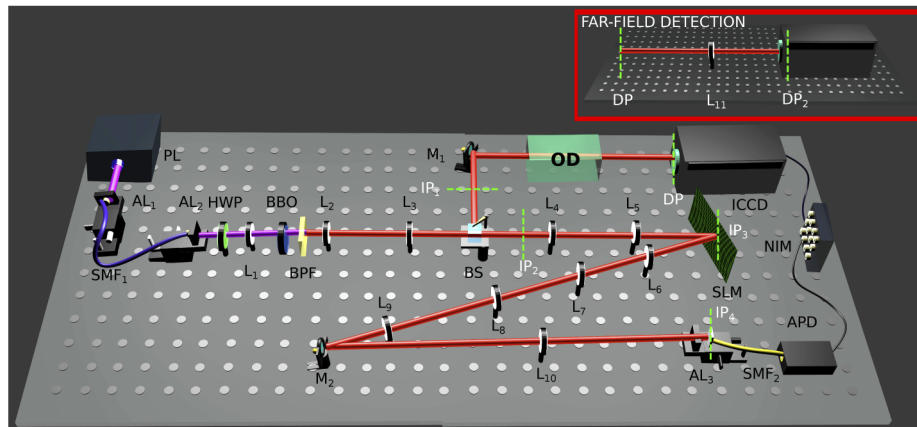


Fig. 1. Experimental setup for producing OAM-entangled photon pairs via collinear type-I SPDC, with projection of the heralding signal photon into a well-defined BG mode and a spatially-resolved detection of the heralded idler photon in the near-field (DP) and the far-field (DP₂ in the inset). The measurement in the near-field provides information about the azimuthal index ℓ , while the spatially-resolved observation of the BG mode in the far-field represents a direct measurement of the scaling factor k_r (see below). The inset shows the additional lens L_{11} required to probe the far-field (DP₂) of the heralded idler photon.

The photon pairs are first spectrally filtered by the BPF element (composed of a long-pass filter which transmits wavelengths $\lambda > 500\text{nm}$, followed by a $810 \pm 5\text{nm}$ band-pass filter), and then split probabilistically into two separate arms by a beamsplitter (BS). The crystal's output plane is imaged onto two identical image planes (IP₁ in the reflected arm, for the idler photon, and IP₂ in the transmitted arm, for the signal photon), using a bifurcated 4f telescope with $2.4\times$ magnification, formed by a plano-convex lens L_2 (with focal length $f_2 = 125\text{mm}$) and a plano-convex lenses L_3 (with $f_3 = 300\text{mm}$).

Our experiment operates as follows (the relevant details are provided below). The signal photon in the transmitted arm is phase modulated (by a spatial light modulator, SLM) and coupled into a single mode fiber (SMF₂), which leads to detection in an avalanche photodiode (APD). The idler photon in the reflected arm is detected, with spatial resolution, by an intensified CCD (ICCD) camera which is time-gated by the electronic pulse produced for each signal-photon detection event at the APD. Note that prior to reaching ICCD, the idler photon is transmitted through an image-preserving delay line (OD) designed to compensate for the insertion delays of the ICCD camera and of the APD (see appendix A). In this manner, we observe the spatial structure of the idler photon in the near and far fields, as heralded by the detection of the phase-modulated signal photon.

The phase mask displayed on the SLM corresponds to the following transmission function [26]

$$T(\rho^\perp, \phi) = \text{sign}[J_\ell(k_r \rho^\perp)] \exp(-i\ell_0 \phi), \quad (6)$$

where ρ^\perp is the radial coordinate, ϕ is the azimuthal angle, and $\text{sign}(\cdot)$ represents the sign function. The effect of the phase $\exp(-i\ell_0 \phi)$ is to suppress an optical vortex phase component in the incoming field proportional to $\exp(i\ell \phi)$ with $\ell = \ell_0$, so that it may couple well into the single mode optical fiber (SMF₂). The result of this phase $\exp(-i\ell_0 \phi)$, acting on its own, is that a field component corresponding to a superposition of BG modes with different scaling factors k_r but the same azimuthal index ℓ_0 is permitted to couple into the fiber. By adding the factor $\text{sign}[J_\ell(k_r \rho^\perp)]$, we are able to effectively also determine a fixed value for the scaling factor k_r . The end result is that the field reflected from the SLM is projected onto a BG mode with user-selected values for *both* the azimuthal index ℓ_0 and for the scaling factor k_r . Note that the slight ellipticity in the modes produced is linked to astigmatism in the overall optical system.

In Fig. 2 we show examples of the phase distribution used on the SLM for all combinations of a selection of ℓ values ($\ell = 1, 5, 8$) and a selection of k_r values ($k_r = 0, 15, 30 \text{ rad/mm}$). As a test of these SLM transmission functions, we couple the beam from a diode laser at 808 nm , in backpropagation through the single mode fiber SMF₂, so that a Gaussian mode reaches the SLM and the resulting intensity pattern is recorded on the crystal plane. These resulting intensity patterns are experimentally recorded, and shown in each of the insets, indicating that the system correctly projects onto the desired mode determined by ℓ and k_r .

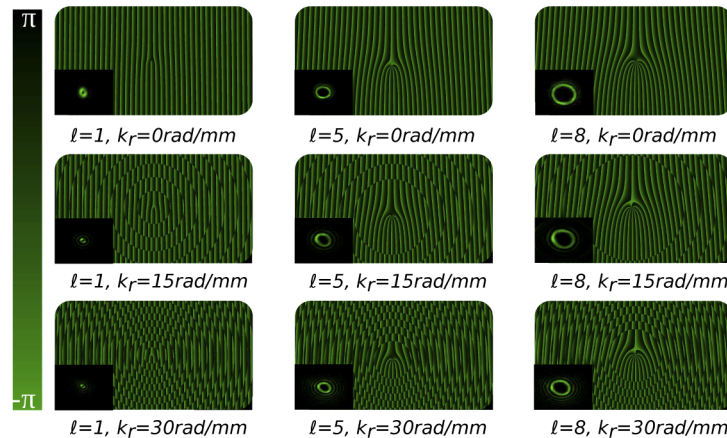


Fig. 2. Phase masks displayed on the SLM used to convert a $k_{rS} = k_r$ and $\ell_S = \ell$ BG signal-photon into a $\ell_S = 0$ Gaussian mode. The inset shows the BG spatial modes defined by the scaling parameter k_r and azimuthal index ℓ obtained, as a test, in backward propagation from the single-mode fiber SMF₂ to the crystal plane.

Returning to the detailed description of our setup, in the transmitted arm, a 4f telescope with $2\times$ magnification – consisting of lenses L_4 (with focal length $f_4 = 100\text{mm}$) and L_5 ($f_5 = 200\text{mm}$) – images the single photon on plane IP_2 to a new plane IP_3 , set to coincide with a spatial light modulator (SLM). Plane IP_3 (phase-modulated by the SLM) is then relayed onto plane IP_4 by three consecutive demagnifying 4f telescopes (with magnifications $0.24\times$, $0.4\times$, and $0.016\times$, respectively), formed by: i) lenses L_6 (with focal length $f_6 = 250\text{mm}$) and L_7 (with $f_7 = 60\text{mm}$), ii) lenses L_8 ($f_8 = 250\text{mm}$) with L_9 ($f_9 = 100\text{mm}$), and iii) lens L_{10} (with $f_{10} = 500\text{mm}$) and aspheric lens AL_3 (with $f_{al3} = 8\text{mm}$). The single photon on plane IP_4 is then coupled into a single mode fiber (SMF₂) with its input plane set to coincide with this plane. The fiber SMF₂ leads to a Si avalanche photodiode (APD) which detects the signal photon.

In the reflected arm, the idler photon on plane IP_1 is transmitted through an image-preserving optical delay line (OD), which introduces a delay of around 115ns (as determined by the insertion delay in both the ICCD and the APD), in order to reach the detection plane (DP) of an ICCD camera (Andor iStar 334T); see appendix A for details of the OD. Since plane DP corresponds to an image of plane IP_1 , placing the detection array of the ICCD camera on DP leads to the detection of the idler photon in the near-field of the crystal. Alternatively, the idler photon's transverse amplitude may be Fourier transformed by transmission through a lens L_{11} (with focal length $f_{11} = 250\text{mm}$) placed a distance f_{11} from DP to define a new plane DP_2 a distance f_{11} from L_{11} , as shown in the inset of Fig. 1. Placing the ICCD on plane DP_2 leads to the detection of the idler photon in the far-field [7]. An important feature of our experiment is the ability to observe the transverse intensity of the heralded idler photon either in the near-field or in the far-field, as selected by the experimenter.

Let us turn to a discussion of how the parameters defining a mode can be obtained experimentally. We note that the radius of the inner-most intensity ring in the near-field intensity pattern (for $|\ell| \geq 1$) is a monotonically increasing function of $|\ell|$ so that it becomes possible with adequate calibration to infer the value of $|\ell|$ in a particular experiment (note that in the case of $\ell = 0$ can be straightforwardly identified since it is the only one which yields an intensity maximum at the origin). We also note that the radius of the single intensity ring appearing in the far-field directly yields the scaling parameter k_r . A Bessel-Gauss mode, as opposed to a Bessel mode, is determined by the width of the Gaussian apodization envelope w_0 , in addition to the ℓ and k_r parameters already discussed. If the w_0 value is required, it can be conveniently inferred from the single intensity ring width in the far-field (as discussed in the theory section above) [32].

Note that a direct determination of the topological charge ℓ of the heralded idler photon, including its sign, could be accomplished through far-field diffraction through a triangular aperture. We followed such a strategy for photons encoded in the LG basis, and of course also could be used in the present case for BG modes [25,32].

In a full experimental run, for each combination of signal-photon projection values ℓ_s and k_{rs} , we record for the idler photon, both, the near-field and far-field intensity patterns (obtained as the spatially-resolved coincidence counting rate). We have performed such an experimental run, for source configuration A (crystal length $L = 2\text{mm}$ and pump spot size $w_0 = 300\text{rad/mm}$), and for $\ell_p = 0$, for all combinations of ℓ_s values within the range $-15 \leq \ell_s \leq 15$ with the following k_{rs} values: $0, 15, 30\text{rad/mm}$. For each combination of k_{rs} and ℓ_s we have collected data over a period of 400s. We present in Figs. 3 (for near-field measurements) and 4 (for far-field measurements) data for a subset of the full resulting measurement set (for ℓ_s values $-10, -5, 0, 5, 10$). The full data, with other ℓ_s and k_{rs} value combinations, is available upon request. In the case of the near-field measurements an inset is included for each measurement, showing the phase distribution programmed on the SLM for that specific measurement (the phase masks are identical for the far-field measurements). The measured near-field and far-field idler-photon intensity patterns, as a function of the user-selected values ℓ_s and k_{rs} , constitute the

direct imaging of the signal-idler correlations which result from the OAM entangled two-photon state.

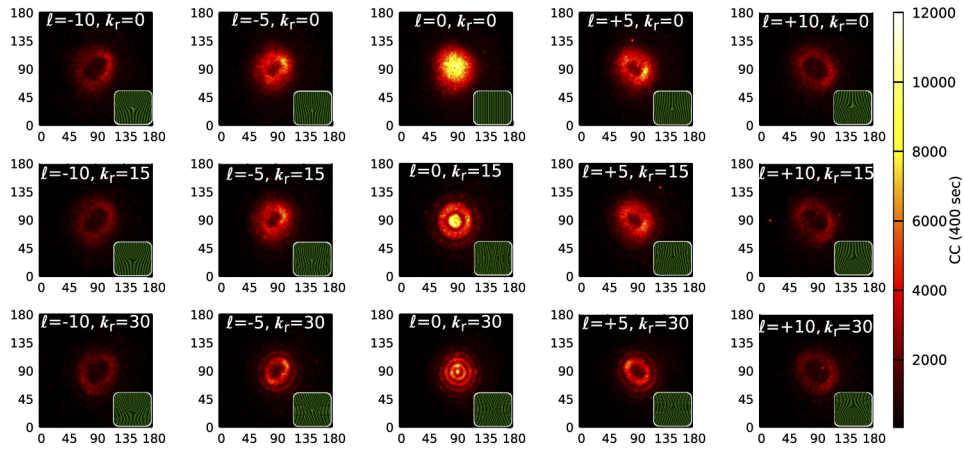


Fig. 3. Spatially-resolved coincidence count rate between the signal photon, projected onto particular k_{rs} and ℓ_s values with the help of a spatial light modulator (SLM) followed by coupling into a single-mode fiber, and the idler photon detected in the near-field by a time-gated ICCD camera. Each plot is labelled by the ℓ_s and k_{rs} (in rad/mm units) values. The axes represent the camera pixels, with the colorbars expressed in coincidence events per 400 seconds. The insets shows the corresponding phase masks (central region shown) displayed on the SLM.

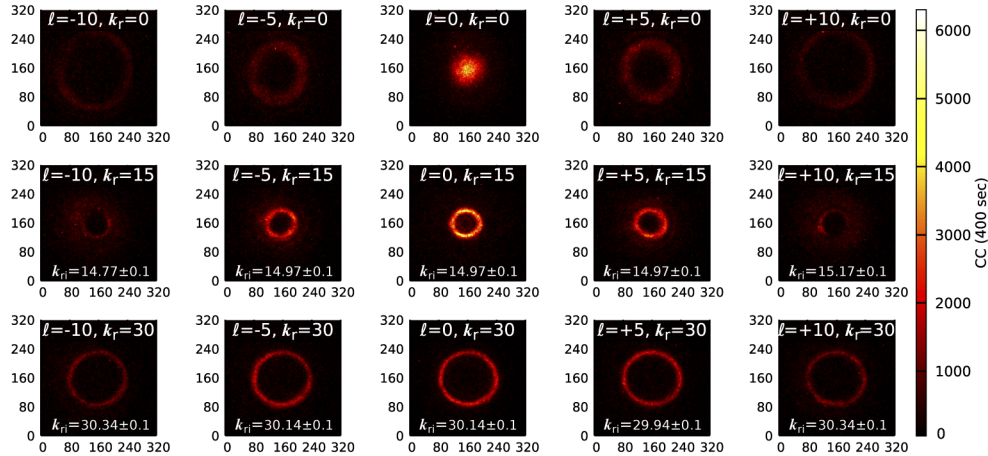


Fig. 4. Spatially-resolved coincidence count rate between the signal photon, projected onto particular k_{rs} and ℓ_s values with the help of a spatial light modulator (SLM) followed by coupling into a single-mode fiber, and the idler photon detected in the far-field by a time-gated ICCD camera. Each plot is labelled by the ℓ_s and k_{rs} (in rad/mm units) values. The axes represent the camera pixels, with the colorbars expressed in coincidence events per 400 seconds. For $k_{rs} \neq 0$ cases, we show the measured k_{ri} values (in rad/mm units) near the bottom of each plot, corresponding well with the k_{rs} projection values used.

From the far-field correlation imaging data (Fig. 4) it is clear that, as expected, each given k_{rs} projection value (with $k_{rs} \neq 0$) defines a family of heralded (idler) modes, each with its angular spectrum in the form of a single intensity ring of radius $k_{ri} = k_{rs}$. Thus, the signal-idler

correlations in the two-photon state imply that the resulting heralded (idler) photon scaling parameter value k_{ri} should be identical to the corresponding heralding (signal) photon value k_{rs} . In each panel of Fig. 4, for $k_{rs} \neq 0$ values, we show near the bottom the experimentally obtained value of k_{ri} , clearly matching well the corresponding k_{rs} value. Note that the ability to determine both indices ℓ_s and k_{rs} for the heralding photon, implies that the heralded photon will be described by a single, well-defined BG mode corresponding to a quantum-mechanically pure state, with indices $\ell_i = -\ell_s$ and $k_{ri} = k_{rs}$.

Let us now turn our attention to the question of how to obtain the spiral spectrum from near-field correlation imaging data (Fig. 3). Indeed, we may directly obtain, for a given selection of scaling factor k_{rs} , the coefficients $|C_{(\ell_s, -\ell_s)}|^2$ from the total intensity summed over all pixels in the data corresponding to a particular ℓ_s . In Fig. 5 we show for source configuration A ($L = 2mm$ and $w_0 = 300\mu m$) the resulting spiral spectrum for the three values of k_{rs} which we have considered ($k_r = 0$, shaded in black, $k_r = 15rad/mm$, shaded in dark blue, and $k_r = 30rad/mm$, shaded in light blue). It may be appreciated that the spiral spectrum becomes flatter (leading to a larger spiral bandwidth) as one increases the value of k_{rs} .

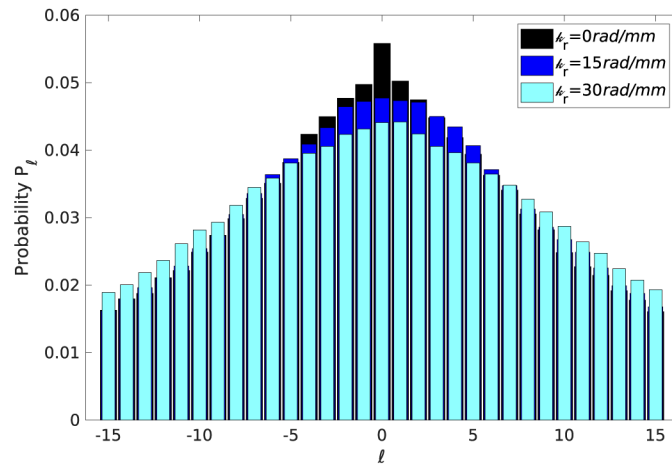


Fig. 5. Measured spiral spectrum $|C_{(l,-l)}|^2$ of the two-photon state (for source configuration A), obtained from the projection of the signal photon to BG modes with three different values of the scaling parameter k_{rs} (0, 15, 30rad/mm) and the azimuthal index ℓ_s .

In Fig. 6 we show, for comparison, the effect on the spiral spectrum of switching from source configuration A ($L = 2mm$ and $w_0 = 300\mu m$), together with $k_{rs} = 0$, to configuration B ($L = 1mm$ and $w_0 = 600\mu m$), together with $k_{rs} = 30rad/mm$. These two situations have been selected since they are highly contrasting, as quantified by the spiral bandwidth. While in the first case the spiral bandwidth (full width at half maximum) is around $\Delta\ell = 16$, in the second case the bandwidth is much larger than the experimentally accessible ℓ range, so that $\Delta\ell \gg 31$. Note that because the radial index for BG modes (scaling parameter) is continuous, in contrast to LG modes for which it is discrete, it may be used to continuously adjust photon pair quantities such as the spiral bandwidth as indeed our experimental results in Figs. 4 and 5 indicate. This could certainly constitute a useful feature for quantum state engineering.

Thus, as known from previous work [26,27], it is possible to engineer the photon-pair quantum state, along with the scaling parameter of the heralding photon, to select the resulting spiral bandwidth over a wide range of possible values.

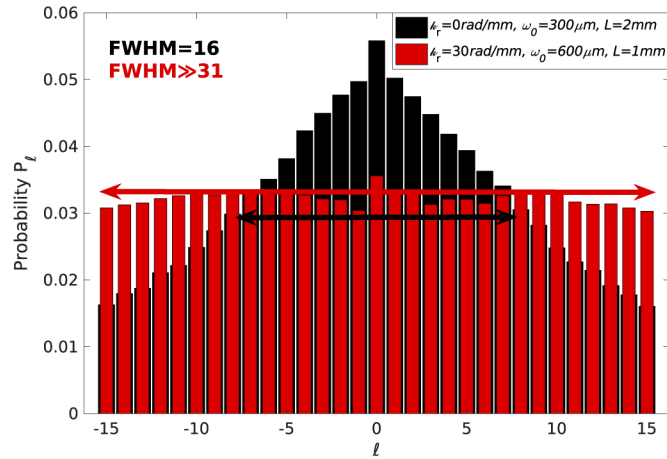


Fig. 6. Comparison of the measured spiral spectrum $|C_{(l,-l)}|^2$ in two situations: i) in black source configuration A with $k_{rs} = 0$ and ii) in red source configuration B with $k_{rs} = 30 \text{ rad/mm}$.

4. Conclusions

We have carried out an experiment in which, for a type-I collinear spontaneous parametric downconversion (SPDC) photon-pair source, we directly image the resulting OAM signal-idler correlations when expressed in the Bessel-Gauss basis. In particular, we project the heralding signal photon onto a Bessel-Gauss (BG) mode with user-selected indices k_{rs} and ℓ_s , and detect the idler photon, with transverse-spatial resolution, in both the near and far fields. The signal-photon projection is accomplished with a spatial light modulator which displays an appropriate phase mask, followed by coupling into a single-mode fiber. The idler photon is detected with spatial resolution by an intensified CCD camera, which is time-gated by the electronic pulse produced by each signal-photon detection event. We show how to retrieve the spiral spectrum from our imaged OAM correlation data, and in addition show how the scaling parameter, along with crystal length and pump focusing strength, can be used to select the resulting spiral bandwidth. Switching to an experimental analysis based on BG, instead of Laguerre-Gauss, modes leads to three distinct advantages: i) the ability to set values for both azimuthal and radial indices, and therefore herald a single photon in a unique BG mode, described by a quantum-mechanically pure state, ii) the ability to experimentally determine both indices solely from the heralded arm: the radial index from a far-field spatially-resolved measurement, and the absolute value of the azimuthal index from a corresponding near-field measurement, and iii) allows us to use the scaling parameter (radial index) as a continuous adjustment for photon-pair properties, in particular for the resulting spiral bandwidth. We believe that these results open up interesting possibilities for future work on the exploitation of the spatial degree of freedom in photon-pair sources.

Appendix A: Image-preserving optical delay line

The image preserving optical delay line (OD in Fig. 1) exploits the same configuration as reported in an earlier work from our group [25]. The delay line, shown in Fig. 7, is formed by eight consecutive $1 \times$ telescopes set in a forward and backward folded-path configuration, propagating the crystal's image plane located at IP_1 up to the ICCD's near-field detection plane defined at DP, introducing a delay of around 115 ns .

The idler photon at IP_1 propagates with the p -polarization transmitted by the polarizing beamsplitter (PBS), placed at the focal plane of the first $1 \times$ telescope, formed by two bi-convex 2''

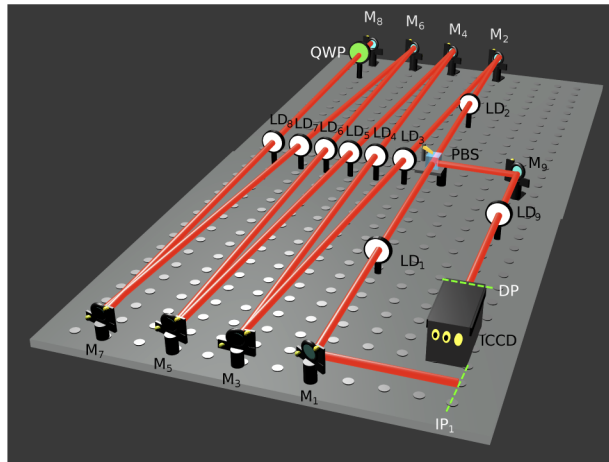


Fig. 7. Details of the image-preserving optical delay line (OD).

diameter, 500mm focal length lenses (LD_1 and LD_2). The next three consecutive $1\times$ telescopes are formed by two bi-convex (2" diameter and 1000mm focal length) lenses, LD_3 to LD_8 . The folded path configuration is accomplished by placing a quarter wave plate (QWP) prior to the last mirror (M_8), flipping the polarization of the idler photon from p to s . After passing again through the three 1000mm $1\times$ telescopes, the s -polarization photon is reflected at the PBS, defining a new optical path including an additional $1\times$ telescope, formed with a 2" diameter 500mm focal length lens (LD_9), relaying the propagated image in a near-field configuration to plane DP.

Funding. Consejo Nacional de Ciencia y Tecnología (Fronteras de la Ciencia grant 217559, grant 293471); Universidad Nacional Autónoma de México (UNAM) (grant IN104418); Air Force Office of Scientific Research (grant FA9550-18-1-0346).

Acknowledgments. We acknowledge support from CONAYCT, Mexico, PAPIIT (UNAM), and AFOSR.

Disclosures. The authors declare no conflicts of interest.

References

- G. Gibson, J. Courtial, M. J. Padgett, M. Vasnetsov, V. Pas'ko, S. M. Barnett, and S. Franke-Arnold, "Free-space information transfer using light beams carrying orbital angular momentum," *Opt. Express* **12**(22), 5448–5455 (2004).
- Daniele Cozzolino, Davide Bacco, Beatrice Da Lio, Kasper Ingerslev, Yunhong Ding, Kjeld Dalgaard, Poul Kristensen, Michael Galili, Karsten Rottwitt, Siddharth Ramachandran, and Leif Katsuo Oxenløwe, "Orbital Angular Momentum States Enabling Fiber-based High-dimensional Quantum Communication," *Phys. Rev. Appl.* **11**(6), 064058 (2019).
- Ding Dong-Sheng, Wei Zhang, Zhou Zhi-Yuan, Shuai Shi, Xiang Guo-Yong, Wang Xi-Shi, Jiang Yun-Kun, Shi Bao-Sen, and Guo Guang-Can, "Quantum Storage of Orbital Angular Momentum Entanglement in an Atomic Ensemble," *Phys. Rev. Lett.* **114**(5), 050502 (2015).
- Shi Bao-Sen, Ding Dong-Sheng, and Wei Zhang, "Quantum storage of orbital angular momentum entanglement in cold atomic ensembles," *J. Phys. B* **51**(3), 032004 (2018).
- Yuan Chen, Jun Gao, Jiao Zhi-Qiang, Ke Sun, Shen Wei-Guan, Qiao Lu-Feng, Hao Tang, Lin Xiao-Feng, and Jin Xian-Min, "Mapping Twisted Light into and out of a Photonic Chip," *Phys. Rev. Lett.* **121**(23), 233602 (2018).
- A. Nicolas, L. Veissier, L. Giner, and J. Laurat, "A quantum memory for orbital angular momentum photonic qubits," *Nat. Photonics* **8**(3), 234–238 (2014).
- R. S. Aspden, D. S. Tasca, A. Forbes, R. W. Boyd, and M. J. Padgett, "Experimental demonstration of Klyshko's advanced-wave picture using a coincidence-count based, camera-enabled imaging system," *J. Mod. Opt.* **61**(7), 547–551 (2014).
- Moreau Paul-Antoine, Ermes Toninelli, Thomas Gregory, S. Aspden Reuben, A. Morris Peter, and J. Padgett Miles, "Imaging Bell-type nonlocal behavior," *Sci. Adv.* **5**(7), eaaw2563 (2019).
- Melanie McLaren and Andrew Forbes, "Digital spiral-slit for bi-photon imaging," *J. Opt.* **19**(4), 044006 (2017).
- Xiaodong Qiu, Dongkai Zhang, Wuhong Zhang, and Lixiang Chen, "Structured-Pump-Enabled Quantum Pattern Recognition," *Phys. Rev. Lett.* **122**(12), 123901 (2019).

11. Hua Chen, Zhou Zhi-Yuan, Alaa Jabbar Jumaah Zangana, Yin Zhen-Qiang, Juan Wu, Han Yun-Guang, Shuang Wang, Li Hong-Wei, He De-Yong, Khasro Tawfeeq Shelan, Shi Bao-Sen, Guo Guang-Can, Wei Chen, and Han Zheng-Fu, "Experimental demonstration on the deterministic quantum key distribution based on entangled photons," *Sci. Rep.* **6**(1), 20962 (2016).
12. V. Sychev Demid, E. Ulanov Alexander, S. Tiunov Egor, Anastasia A. Pushkina, A. Kuzhamuratov, Novikov Valery, and A. I. Lvovsky, "Entanglement and teleportation between polarization and wave-like encodings of an optical qubit," *Nat. Commun.* **9**(1), 3672 (2018).
13. S. S. Barnett Franke-Arnold, "Two-photon entanglement of orbital angular momentum states," *Phys. Rev. A* **65**(3), 033823 (2002).
14. H. Arnaut and G. Barbosa, "Orbital and intrinsic angular momentum of single photons and entangled pairs of photons generated by parametric down-conversion," *Phys. Rev. Lett.* **85**(2), 286–289 (2000).
15. A. Mair, A. Vaziri, G. Weihs, and A. Zeilinger, "Entanglement of the orbital angular momentum states of photons," *Nature* **412**(6844), 313–316 (2001).
16. A. M Yao, "Angular momentum decomposition of entangled photons with an arbitrary pump," *New J. Phys.* **13**(5), 053048 (2011).
17. A. H. Ibrahim, F. S. Roux, M. McLaren, T. Konrad, and A. Forbes, "Orbital-angular-momentum entanglement in turbulence," *Phys. Rev. A* **88**(1), 012312 (2013).
18. V. D. Salakhutdinov, E. R. Eliel, and W. Löffler, "Full-Field Quantum Correlations of Spatially Entangled Photons," *Phys. Rev. Lett.* **108**(17), 173604 (2012).
19. R. Fickler, M. Krenn, R. Lapkiewicz, S. Ramelow, and A. Zeilinger, "Real-time imaging of quantum entanglement," *Sci. Rep.* **3**(1), 1914 (2013).
20. B. Jack, J. Leach, J. Romero, S. Franke-Arnold, M. Ritsch-Marte, S. M. Barnett, and M. J. Padgett, "Holographic ghost imaging and the Violation of a Bell Inequality," *Phys. Rev. Lett.* **103**(8), 083602 (2009).
21. A. C. Dada, J. Leach, G. S. Buller, M. J. Padgett, and E. Andersson, "Experimental high-dimensional two-photon entanglement and violations of generalized Bell inequalities," *Nat. Phys.* **7**(9), 677–680 (2011).
22. J. Leach, B. Jack, J. Romero, M. Ritsch-Marte, R. W. Boyd, A. K. Jha, S. M. Barnett, S. Franke-Arnold, and M. J. Padgett, "Violation of a Bell inequality in two-dimensional orbital angular momentum state-spaces," *Opt. Express* **17**(10), 8287–8293 (2009).
23. E. Yao, S. Franke-Arnold, J. Courtial, M. J. Padgett, and S. M. Barnett, "Observation of quantum entanglement using spatial light modulators," *Opt. Express* **14**(26), 13089–13094 (2006).
24. M. Miatto Filippo, M. Yao Alison, and M. Barnett Stephen, "Full characterization of the quantum spiral bandwidth of entangled biphotons," *Phys. Rev. A* **83**(3), 033816 (2011).
25. Ibarra-Borja Zeferino, Carlos Sevilla-Gutierrez, Roberto Ramírez-Alarcón, Zhan Qiwen, Hector Cruz-Ramírez, and Alfred B. U'Ren, "Direct observation of OAM correlations from spatially entangled bi-photon states," *Opt. Express* **27**(18), 25228–25240 (2019).
26. M. McLaren, M. Agnew, J. Leach, F. S. Roux, M. J. Padgett, R. W. Boyd, and A. Forbes, "Entangled Bessel-Gaussian beams," *Opt. Express* **20**(21), 23589–23597 (2012).
27. Melanie McLaren, Jacqueline Romero, J. Padgett Miles, S. Roux Filippus, and Andrew Forbes, "Two-photon optics of Bessel-Gaussian modes," *Phys. Rev. A: At., Mol., Opt. Phys.* **88**(3), 033818 (2013).
28. Zhao Shengmei, Zhang Wenhao, Wang Le, Li Wei, Gong Longyan, Cheng Weiwen, Chen Hanwu, and Gruska Jozef, "Propagation and self-healing properties of Bessel-Gaussian beam carrying orbital angular momentum in an underwater environment," *Sci. Rep.* **9**(1), 2025 (2019).
29. J. P. Torres, A. Alexandrescu, and Torner Lluís, "Quantum spiral bandwidth of entangled two-photon states," *Phys. Rev. A* **68**(5), 050301 (2003).
30. Clara I. Osorio, Molina-Terriza Gabriel, and P. Torres Juan, "Correlations in orbital angular momentum of spatially entangled paired photons generated in parametric down-conversion," *Phys. Rev. A* **77**(1), 015810 (2008).
31. C. Gutierrez-Vega and Miguel A. Bandres, "Helmholtz Gauss waves," *J. Opt. Soc. Am. A* **22**(2), 289–298 (2005).
32. Julio C. Gutiérrez-Vega and Miguel A. Bandres, "Classical to quantum transfer of optical vortices," *Opt. Express* **22**(17), 20027–20037 (2014).
33. Verónica Vicuña-Hernández, Héctor Cruz-Ramírez, Roberto Ramírez-Alarcón, and Alfred B. U'Ren, "Observation of non-diffracting behavior at the single-photon level," *Opt. Express* **20**(28), 29761–29768 (2012).